Article

A Comprehensive Comparison among Capacitive, Thermodynamic, and Drift−Diffusion Models for Steady-State Responses of Nanostructured Organic Electrochemical Transistors

Andres Unigarro and Florian Günther*

Read Online

ACCESS | Metrics & More | Article Recommendations | SI Supporting Information

ABSTRACT: Organic electrochemical transistors (OECTs) have garnered significant interest in organic electronics due to their fast response, high transconductance, low operating voltage, and versatile fabrication processes. Despite their successful application in various devices, the theoretical understanding of OECTs remains incomplete, particularly regarding the nanoscale interaction between ionic and electronic transport within the organic mixed ionic−electronic conductors (OMIECs) used in these devices. This work introduces a drift−diffusion model that addresses the limitations of existing theoretical frameworks. An analytical expression for the steady-state current in the OECTs is derived, which accounts for both electrical parameters (e.g., gate and drain voltages) and material properties (e.g., salt concentration in the electrolyte). The applicability of our model is validated through comparison with experimental data, revealing new insights into the interplay of various factors affecting the OECT performance. Additionally, we revisit and extend the well-established Bernards−Malliaras (BM) model to cover a broader range of operating conditions, as well as a thermodynamic model. We show that correct usage of the theoretical formulas yields agreement with experimental curves for all presented models, rendering the match itself an insufficient proof of the underlying theory. We set up interconversion formulas between the parameters of the different model approaches and analyze what this implies for their meaning, especially because all show good agreement with the experiment, although based on quite different fundamentals. This comparative analysis provides a deeper understanding of how different components contribute to device operation, offering guidance for the targeted optimization of OECT materials and design with a focus on the exploiting nanoscale phenomena.

KEYWORDS: *organic electrochemical transistors, mixed ionic−electronic conductors, theoretical modeling, transfer and output characteristics, drift−diffusion*
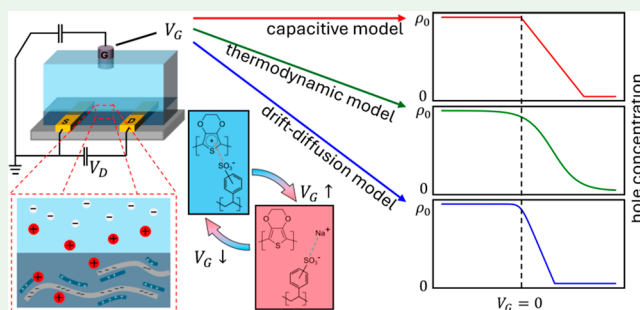
1. INTRODUCTION

Among the devices developed within the field of organic electronics, organic electrochemical transistor (OECT) technology has attracted widespread interest due to features such as fast response speed, high transconductance, low driving voltage, and versatility in terms of fabrication processes.[1−3] To date, OECTs have been successfully implemented, e.g., as circuit elements,[4] neuromorphic devices,[5] batteries,[6] and sensing elements.[7] The typical architecture of an OECT consists of an organic mixed ionic−electronic conductor (OMIEC) in contact with an electrolyte acting as a reservoir of ions, in which an electrode (the gate) is immersed; see Figure 1. Two further electrodes (referred to as the drain and source) are contacted with the OMIEC, defining a channel through which an electric current I_D can flow once a drain voltage V_D is applied. When a voltage V_G is applied between the gate and source, ions migrate from the electrolyte into the OMIEC material, causing a modification of the electronic charge charier density ρ, and thus the electronic current I_D

changes.[8,9] This process is called electrochemical doping, "electrochemical" due to the electrochemical process involved and "doping" in analogy to the insertion of additional charges in inorganic semiconductors.

In the last years, novel polymeric materials with mixed conductor properties have been synthesized and characterized for the use of electrochemical applications.[10,11] One of the most efficient ones in terms of practical applications is the polymeric blend PEDOT:PSS,[3] in which the conjugated polymer poly-3,4-ethylendioxythiophen (PEDOT) is p-doped and counter-balanced by negative polystyrenesulfonate (PSS)
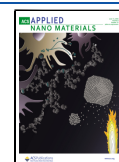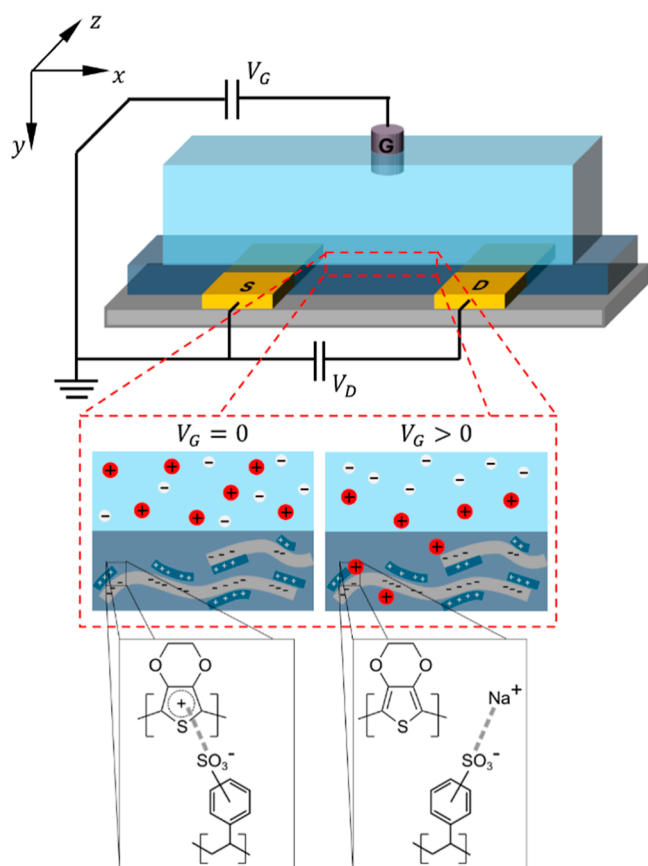
Figure 1. Schematic representation of a depletion-mode OECT based on PEDOT:PSS.

units, see the lower-left illustration in Figure 1. Depending on the deposition technique, PEDOT:PSS forms films with different nanostructured morphologies. Furthermore, the material exhibits nanoscale phase separation between PEDOT and PSS domains, both of which critically impact its electrochemical and transport behavior.[12,13] In contrast to doping with small compounds, PSS is a polyelectrolyte, where the ionic charges are bonded to a macromolecule and therefore largely immobile. PEDOT:PSS is soluble in water and presents good film-forming abilities, an intrinsically high work function, and good physical and chemical stability under ambient conditions.[6] Furthermore, conductivities up to 1×10^3 S cm^{-1} have been reported in the literature.[14] When the OMIEC film of an OECT channel consists of predoped material such as PEDOT:PSS, the device works in so-called depletion mode. This means that the ions injected upon application of a gate voltage do not change the doping state of the semiconductor directly but rather shield the prior existing counter charges (in the case of PEDOT:PSS, the PSS anions), see the lower-right illustration in Figure 1. This leads to a reduction in the doping level of the OMIEC, which is called dedoping. Hence, in depletion-mode OECTs, the channel current decreases with an applied gate voltage.[3,15]

Although various advances and performance improvements of OECTs have been reported in the past years, these achievements were mostly based on more controlled device fabrication or the trial-and-error use of new synthesized materials.[16−21] A targeted material design suggested by a profound theory of the working mechanisms of OECTs is, in fact, still missing. Therefore, it is necessary to explore and

develop new characterization and data processing methods through theoretical modeling of experimental data.

One of the first but still most widely used OECT models was published by Bernards and Malliaras, based on which they developed analytical expressions for $I_D(V_G, V_D)$ under certain conditions.[8] Their approach involves the description of ion uptake by the OMIEC as a capacitive process that scales with the volume of the OMIEC, resulting in the so-called volumetric capacitance c^*. Its product with the electronic mobility Λ_h (as in other works,[22] this uncommon notation is used to avoid confusion with the chemical potential μ discussed below), of the OMIEC is considered the figure of merit and is therefore an important benchmark quantity of an OECT. The Bernards−Malliaras (BM) model was initially formulated to describe the output characteristics of PEDOT:PSS-based depletion-mode transistors, such that the obtained expressions were limited to cases where $V_G > 0$. In the past decade, more refined approaches have been developed looking for a more accurate description of the internal physical processes occurring inside an OECT during its operation including modifications to accumulation-mode OECTs,[23] considering change of mobility due to doping,[24] focusing on transfer curves[25] and others, but keeping the volumetric capacitance as a parameter. Furthermore, all of these works consider the injection of ions into the OMIEC as an exclusive consequence of the effect of the electric field upon an applied gate voltage. But ion migration also occurs in the form of diffusion generated by concentration gradients (Fick's law) or, more specifically, due to the gradient in chemical potential. With the aim to model the transient response of OECTs, Coppedè et al. derived a drift−diffusion model that yielded an analytical expression of the transient current with the diffusivity being the only unknown parameter.[26] Comparing the model to experimental measurements, Coppedè et al. concluded on different diffusion properties when different cations are used in the electrolyte solution. Their model, however, is based on unphysical boundary conditions, which renders the applicability rather questionable. For example, the model is based on open boundary conditions, which means that it is incapable of describing steady-state conditions. In contrast to capacitive and drift−diffusion models, other works focus on the (de)doping reaction rather than the ion migration to describe the change of conductivity of the semiconducting layer. Very recently, Cucchi et al. presented a model based on thermodynamic and equilibrium chemistry principles which yielded an expression for steady-state current of OECTs.[22]

In this work, we present an approach based on the drift−diffusion formulation, which originates from the aim to correct the unphysical boundary conditions of Coppedè's model to describe the transient response.[26] In doing so, we obtained an analytical description of the steady-state current as a function of the electrical conditions V_G and V_D but also of the material parameters like the salt concentration in the electrolyte, which has not been reported before. We furthermore review the Bernards−Malliaras (BM) model in more detail and complete it toward the full range of gate and drain voltage. To assess the applicability of the discussed models, we compare the experimental curves and derive intercorrelation equations between the models. In doing so, our work provides the possibility to assess which properties of the individual components must be optimized to obtain improved OECT performances. Although our model also allows the formulation of transient characteristics, in here, we will focus on the steady-

state limits and compare the obtained results to the existing models from literature. A detailed presentation of the transient description will be reported elsewhere.

2. OECT MODELS

The following expressions are derived for p-type depletion-mode OECTs but can easily be reformulated to n-type or accumulation-mode transistors.[8] Starting from the simple assumption that under steady-state conditions, the source–drain current is dominated by the hole transport in the semiconducting layer, the current density $\vec{j}_h$ is given by using Ohm's law:

$$\vec{j}_h(\vec{r}) = \sigma_h(\vec{r})\vec{E}(\vec{r}) = e\Lambda_h\rho_h(\vec{r})\frac{\partial V_{ch}}{\partial \vec{r}} \tag{1}$$

Here, $\sigma_h(\vec{r})$ is the hole conductivity of the semiconductor film at position $\vec{r}$, $\vec{E}(\vec{r}) = \frac{\partial V_{ch}}{\partial \vec{r}}$ is the electric field associated with the change of electric potential $V_{ch}(\vec{r})$ along the channel, e is the elementary charge, Λ_h is the hole mobility, and $\rho_h(\vec{r})$ is the hole concentration. Treating Λ_h as a constant, the change of σ with the channel position $\vec{r}$ is solely described by $\rho_h(\vec{r})$. For reference and clarity, a summary of all utilized symbols is given in Supporting Information Section S1, sorted into physical constants (Table S1), general quantities (Table S2), device geometry (Table S3), and electrical quantities (Table S4), as well as into model-specific quantities of the Bernards–Malliaras model (Table S5), the thermodynamic model (Table S6), and the drift–diffusion model (Table S7).

Under steady-state conditions, a homogeneous current density in the channel direction can be assumed such that the source–drain current I_D is given as

$$I_D = \int \vec{j}_h \, d\vec{A} = wd_{sc}[\vec{j}_h \cdot \vec{e}_x] \tag{2}$$

Here, and in the following, the semiconductor film thickness and channel width are referred to as d_{sc} and w, respectively, whereas $\vec{e}_x$ is the unit vector in the source–drain direction. Expressing the hole concentration as a function of channel potential V_{ch} provides

$$I_D = wd_{sc}e\Lambda_h\rho_h\left[\frac{\partial V_{ch}}{\partial \vec{r}} \cdot \vec{e}_x\right] = wd_{sc}e\Lambda_h\rho_h(V_{ch}, V_G)\frac{dV_{ch}}{dx} \tag{3}$$

Placing the source contact where $V_{ch} = 0$ at $x = 0$ and the drain contact with $V_{ch} = V_D$ at $x = l$ (with l being the channel length), one finds

$$I_D = G\int_0^{V_D}\frac{\rho_h(V_{ch})}{\rho_0}\,dV_{ch} \tag{4}$$

with

$$G = e\Lambda_h\rho_0\frac{wd_{sc}}{l} \tag{5}$$

being the conductance of the entire channel, and ρ_0 is the hole concentration of ungated channel (pristine PEDOT:PSS without dedoping ions). Since all models, which will be discussed in the following, assume ideal semiconducting channels, meaning a constant channel intersection with width w and thickness d_{sc}, homogeneous intrinsic hole concentration ρ_0, and constant mobility Λ_h, the conductance G is a device-

specific constant, and the change in I_D is solely due to the dedoping of the semiconducting material. To investigate this variation, we introduce the dimensionless scaling factor

$$\alpha(V_D, V_G) = \frac{I_D(V_D, V_G)}{GV_D} \tag{6}$$

which reflects the current I_D normalized to the current of the ungated film. This quantity is independent of the device geometry parameters and the charge carrier mobility and expresses how the electrical conditions vary the film conductance between zero and G. The limit $V_D \to 0$ is particularly interesting, as it corresponds to the case where the semiconducting film is at a constant potential. Evaluating this limit in eq 6, one finds

$$\alpha_{V_D \to 0} = \frac{\rho_h(V_{ch} = 0, V_G)}{\rho_0} \tag{7}$$

This means that the quantity $\alpha_{V_D \to 0}$ represents the dependence of hole concentration as a function of the gate voltage, normalized to the maximal hole concentration ρ_0.

2.1. Bernards–Malliaras Model. To express the dependence of ρ_h on the potentials applied at the electrodes as well as material parameters of the semiconductor, Bernards and Malliaras used the simple assumption that each cation that is injected into the semiconducting film pairs with a PSS⁻ unit shielding the charge responsible to stabilize the (bi)polaron of PEDOT, see Figure 1. Therefore, the hole concentration depends linearly on the total ion charge Q_{ion} that enters the semiconducting volume v at channel position $\vec{r}$

$$\rho_h^{BM}(\vec{r}) = \rho_0\left(1 - \frac{Q_{ion}(\vec{r})}{e\rho_0 v(\vec{r})}\right) \tag{8}$$

Note that eq 2 only holds within the limits $0 < Q_{ion} < ev\rho_0$. To model the dependence of Q_{ion} on the electrical potentials applied at the device contacts, the BM model treats the transition of ions from the electrolyte into each semiconductor volume element v as the charging of a capacitor of capacitance C:

$$Q_{ion}(\vec{r}) = C(V_G - V_{ch}(\vec{r})) \tag{9}$$

Inserting eq 9 into eq 8 yields a dependence of the hole concentration on the channel voltage:

$$\rho_h^{BM}(V_{ch}) = \rho_0\left(1 - \frac{V_G - V_{ch}}{V_P^{BM}}\right) \tag{10}$$

with

$$V_P^{BM} = \frac{e\rho_0 v}{C} = \frac{e\rho_0}{c^*} \tag{11}$$

being the pinch-off voltage at which the semiconductor is fully dedoped and the hole concentration has vanished. Equation 5 introduces the volumetric capacitance $c^* = \frac{C}{v}$, which is often considered to be an important parameter of OECTs as it characterizes the uptake of ions in the semiconductor volume. In fact, the product of (hole) mobility and volumetric capacitance is considered to be the figure of merit of OECTs.[23]

Using eq 10, an analytical expression for I_D as a function of the electrical conditions V_D and V_G can be obtained. One should emphasize, however, that for the integration of eq 4

Table 1. Overview of the Nine Operational Regimes of the BM Model

regime		I_D^{BM}	$\alpha^{BM}(V_D, V_G)$	$\alpha_{V_D\to 0}^{BM}(V_G)$	ref
I	$V_D < 0 < V_{sat}^{BM} < V_G$ $0 < V_D < V_{sat}^{BM} < V_G$	0	0	0	8
II	$0 < V_{sat}^{BM} < V_D < V_G$	$G\dfrac{(V_D - V_G + V_P^{BM})^2}{2V_P^{BM}}$	$\dfrac{(V_D - V_G + V_P^{BM})^2}{2V_P^{BM}V_D}$		
III	$0 < V_{sat}^{BM} < V_G < V_D$	$G\left[\dfrac{V_P^{BM}}{2} + V_D - V_G\right]$	$\left[\dfrac{V_P^{BM} - 2V_G}{2V_D} + 1\right]$		
IV	$V_D < V_{sat}^{BM} < 0 < V_G$	$-G\dfrac{(V_G + V_P^{BM})^2}{2V_P^{BM}}$	$-\dfrac{(V_G + V_P^{BM})^2}{2V_P^{BM}V_D}$		8, 25
V	$V_{sat}^{BM} < V_D < 0 < V_G$ $V_{sat}^{BM} < 0 < V_D < V_G$	$G\left(1 - \dfrac{2V_G - V_D}{2V_P^{BM}}\right)V_D$	$\left(1 - \dfrac{2V_G - V_D}{2V_P^{BM}}\right)$	$\left(1 - \dfrac{V_G}{V_P^{BM}}\right)$	8, 25
VI	$V_{sat}^{BM} < 0 < V_G < V_D$	$G\left(1 - \dfrac{V_G^2}{2V_P^{BM}V_D}\right)V_D$	$\left(1 - \dfrac{V_G^2}{2V_P^{BM}V_D}\right)$		8
VII	$V_D < V_{sat}^{BM} < V_G < 0$	$G\left(V_G - \dfrac{V_P^{BM}}{2}\right)$	$\dfrac{1}{V_D}\left(V_G - \dfrac{V_P^{BM}}{2}\right)$		25
VIII	$V_{sat}^{BM} < V_D < V_G < 0$	$G\left(1 + \dfrac{(V_D - V_G)^2}{2V_P^{BM}V_D}\right)V_D$	$\left(1 + \dfrac{(V_D - V_G)^2}{2V_P^{BM}V_D}\right)$		25
IX	$V_{sat}^{BM} < V_G < V_D < 0$ $V_{sat}^{BM} < V_G < 0 < V_D$	GV_D	1	1	25
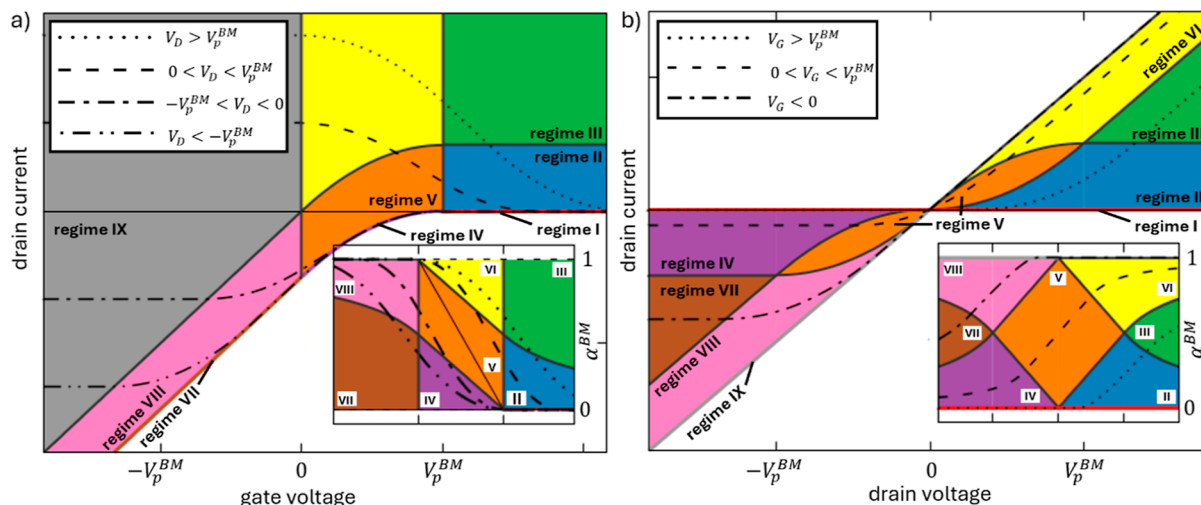
Figure 2. Color chart of transfer (a) and output (b) plots displaying the nine different operational regimes of depletion-mode OECTs according to the BM model. Dashed/dotted curves exemplify representative curves for the different electronic conditions. Inset figures present the corresponding regimes and curves for the dimensionless parameter α, which represents the relative film conductivity, see eq 9.

over V_{ch}, different scenarios must be considered, since eq 10 only holds for $V_G - V_P^{BM} < V_{ch} < V_G$, which is often not properly done. Since for p-type depletion-mode OECTs it holds $V_P^{BM} > 0$, the saturation voltage

$$V_{sat}^{BM} = V_G - V_P^{BM} \qquad (12)$$

is always smaller than V_G. But without further specification, V_{sat}^{BM} and V_G can be positive or negative depending on the choice of V_G with respect to V_P. Table 1 presents all possibilities of how the sequence of $V_S = 0$, V_G, V_D, and V_{sat} affects the expressions of the source drain current. The detailed

derivation of the expressions is presented in Supporting Information, Section S2. Figure S1 illustrates the doping level along the semiconductor channel schematically regarding the nine regimes.

As the original work of Bernards and Malliaras was focused on PEDOT:PSS-based OECTs, which usually possess large V_P due to the large intrinsic hole concentration ρ_0, only the scenarios with $V_P^{BM} > V_G > 0$, i.e., regimes IV−VI, were discussed in detail. In the work of Nissa et al.,[25] the BM model was extended to scenarios with $-V_P^{BM} < V_G < V_P^{BM}$ corresponding to regimes VII−IX in Table 1. The scenario of complete dedoping at $V_G \geq V_P^{BM}$ was only mentioned by

Bernards and Malliaras as a hypothetical scenario because the high gate voltages needed for complete dedoping would lead to other physical effects in the device (e.g., electrolysis of the electrolyte solution), rendering the model inapplicable for experimental devices. Using novel materials with advanced conditions, however, might allow one to obtain devices that can operate under these conditions. For example, very recently, Barbosa et al.[27] presented a work in which low-conductive PEDOT:PSS inks were synthesized and successfully used as postsynaptic electrodes in a neuromorphic device. In that work, OECT data is presented with vanishing source−drain current for $V_G > 0.3$ V. For this reason, we also present the cases with $V_G > V_p^{BM}$ (regimes I−III), which have not been discussed in literature before.

Figure 2 schematically illustrates the formation of the drain current through the distinct regimes, represented by a color map. Transfer curves (Figure 2a), i.e., when V_D is constant, trace S-shaped curves as exemplified by the black dashed lines for different choices of the drain voltage with respect to the pinch-off voltage. Each of those curves is constituted by a sequence of constant, quadratic, linear, quadratic, and constant functions. The constant regions can be attributed to the off-state and the on-state (regimes I and IX, respectively), where in the former the OMIEC is fully dedoped and therefore insulating, whereas in the latter the hole concentration equals the intrinsic hole concentration ρ_0 within the whole channel, such that the OECT possesses Ohmic behavior. In the case of output curves (Figure 2b), they are composed of a sequence of constant, quadratic, and linear functions. Again, the specific ranges for each shape depend on the relationship between V_G and V_p^{BM}.

2.2. Thermodynamic Model.
Although the BM model and its extensions have been used extensively to characterize real OECTs, they do not incorporate the actual process of the electrochemical (de)doping reaction. Aiming at formulating a model of the OECTs based on this phenomenon, researchers have approached the problem from a thermodynamic (TD) perspective. For example, Prigodin and colleagues presented a study in which an expression for the drain current was obtained under the assumptions of a constant electrochemical potential of ions within the channel.[28] This means that the ions are at equilibrium along the semiconducting material. Although their expressions were able to describe the OECT behavior, the authors commented that the model is not sufficient to explain the full operation of the device. In a more recent work, Cucchi et al. considered PEDOT:PSS-based OECTs and the chemical equilibrium between PEDOT[0] and PEDOT[+] according to thermodynamic principles. Upon a change in the gate voltage, the perturbation of this equilibrium is considered. Analyzing expressions for the Gibbs energy allowed them to describe the hole density in the channel as a function of the difference between the electrochemical potential of doped (μ^{p+}) and neutral state (μ^{p0}) of PEDOT. Neglecting the enthalpy contribution of the mixing of PEDOT[0] and PEDOT[+], the hole concentration was derived as

$$\rho_h^{TD}(V_{ch}) = \rho_0 \left(1 - \frac{1}{Z \exp(-\beta(V_G - V_{ch})) + 1} \right) \quad (13)$$

resulting in the source drain current

$$I_D^{TD}(V_G, V_D) = \frac{G}{\beta} \ln \left(\frac{Z \exp(-\beta(V_G - V_D)) + 1}{Z \exp(-\beta V_G) + 1} \right) \quad (14)$$

where $\beta = e/k_b T$, $Z = \exp\left(\frac{(\mu^{p+} - \mu^{p0})}{k_b T} \right)$, with T being the absolute temperature and k_b the Boltzmann's constant. It is noteworthy to remark that a similar expression was previously found by Prigodin et al.[28]

The fundamental feature of eq 14 is that the dependence of the current as a function of the gate and drain voltages is given by the nested logarithmic and exponential terms. That way, in contrast to the BM model, the separation into on-state, off-state, and transition regimes emerges intrinsically; see Figure S2. Note that for certain limits, where the term inside the logarithm is close to one, the thermodynamic model is asymptotically linear or constant.

In their work, Cucchi et al. introduce a further parameter to obtain proper agreement between the theoretical expression and experimental data. They claim that as a consequence of the potential drop across the electrolyte, the effective potential acting on the semiconducting film is only a fraction of the applied gate voltage. For this reason, they introduce the factor $0 < \gamma < 1$ and substitute γV_G for V_G in eq 14. While trying to confirm their results, we conclude that the formula presented in their work was not the one used to make the fit. Instead, one in which factor γ is also applied to the drain voltage was implemented. For this case, however, eq 14 must be multiplied by $1/\gamma$ in order to ensure that for the limit $V_G \rightarrow -\infty$, the conductance equals that of the intrinsic film. Hence, the proper expression of the drain current should be

$$I_D^{TD}(V_G, V_D) = \frac{G}{\gamma \beta} \ln \left(\frac{Z \exp(-\gamma \beta(V_G - V_D)) + 1}{Z \exp(-\gamma \beta V_G) + 1} \right) \quad (15)$$

Note that in this expression, the factor γ rather applies to $\beta = \frac{e}{k_b T}$ than to gate and drain voltages. This allows for an alternative interpretation of the meaning of γ than the one raised by Cucchi et al. Since ions in solution are typically surrounded by a solvation shell, their charges are partially shielded, to which γ can be attributed. A more detailed discussion of the choice of γ is provided in Supporting Information, Section S3.

For the TD model, the dimensionless scaling factor α introduced in eq 6 can be written as

$$\alpha^{TD} = \frac{1}{\gamma \beta V_D} \ln \left(\frac{Z \exp(-\beta \gamma(V_G - V_D)) + 1}{Z \exp(-\beta \gamma V_G) + 1} \right) \quad (16)$$

In the limit $V_D \rightarrow 0$, α^{TD} becomes

$$\alpha_{V_D \rightarrow 0}^{TD} = \frac{Z}{Z + e^{\beta \gamma V_G}} \quad (17)$$

Although key features of OECTs, e.g., the saturation in on-state and off-state, emerge naturally from this TD model, simplifications such as uniform dedoping along the channel needed to be made to obtain the analytical expression of eq 16. This way, some device features, such as the type of electrolyte or its ion concentration, that evidently impact the performance and the characteristics of OECTs are not able to be represented by that model.[21,29−33] Including the effects of enthalpy contributions, Cucchi et al. were able to incorporate such effects in their model.[22] In this case, however, the equation for the drain current cannot be solved analytically, and numerical methods must be used. While an improvement in the agreement with experimental results was obtained, the

authors concluded that the driving force behind the OECT operation is entropy, and enthalpic terms only produce small perturbations in the results, suggesting that eq 10 is sufficient to characterize the functioning of OECTs.

2.3. Drift−Diffusion Model. In order to find a more fundamental description of the ionic charge Q_{ion} than that of the capacitive approach of the BM model (eq 3), an expression of ion concentration profile $\psi(\vec{r}, t)$ within the whole OECT device is needed. As before in the BM and TD models, individual slices of width Δx at channel position x are considered, and homogeneity in the z-direction (constant width w) is assumed. This reduces the system to a one-dimensional problem in the y-direction. Under these assumptions, the net flux J of the ion concentration (here, we use capital letters to distinguish the ion flux from the hole current density j_h) at any position y along the slice to a given time t can be expressed as[34]

$$J(y, t) = -\frac{D(y)}{RT}\psi(y, \tau)\frac{\partial \overline{\mu}}{\partial y} \tag{18}$$

Here, $D(y)$ is the diffusivity of the ion in the system and $\overline{\mu}(y)$ is the electrochemical potential. The latter is defined as[34]

$$\overline{\mu}(y, t) = \mu(y, t) + zF\Phi(y) \tag{19}$$

where $\mu(y, t)$ is the chemical potential, which can be written as[34]

$$\mu(y, t) = \mu_0(y) + RT \ln \psi(y, t) \tag{20}$$

In eqs 18−20, t refers to time, R is the universal gas constant, F is Faraday's constant, z is the ionic charge number, and $\Phi(y)$ is the electrical potential. In contrast to the TD model, μ_0 represents the standard chemical potential of the ions in the medium and not the electrochemical potential of different doping states of PEDOT. Assuming conservation of total ion concentration in each slice, the continuity equation

$$\frac{\partial \psi(y, t)}{\partial t} = -\frac{\partial J(y, t)}{\partial y} \tag{21}$$

must hold.

2.3.1. Coppedè−Villani−Gentile (CVG) Model. Inserting eqs 19 and 20 into eq 18 under the assumption of constant standard chemical potential μ_0 results in the one-dimensional Nernst−Plank equation.[26]

$$J(y, t) = -D(y)\left(\frac{\partial \psi}{\partial y} - \frac{zF}{RT}E_y\psi\right) \tag{22}$$

Assuming a homogeneous diffusion coefficient and constant E_y, the substitution of eq 22 into eq 21 results in the governing equation for the temporal evolution of the ion concentration profile $\psi(y, t)$:

$$\frac{\partial \psi(y, t)}{\partial t} = D\frac{\partial^2 \psi}{\partial y^2} - \nu\psi \tag{23}$$

with drift coefficient $\nu = \frac{zF}{RT}E_y$. Since eq 23 has the form of a one-dimension convection−diffusion solute transport equation, the Coppedè−Villani−Gentile (CVG) model uses the analytical solution

$$\psi(y, t) = \frac{\psi_0}{2}\left(\text{erf}\left(\frac{y - \nu t}{2\sqrt{Dt}}\right) - \text{erf}\left(\frac{y - d_{el} - \nu t}{2\sqrt{Dt}}\right)\right.$$
$$\left. + \exp\left(\frac{\nu x}{D}\right)\left[\text{erf}\left(\frac{y + \nu t}{2\sqrt{Dt}}\right) - \text{erf}\left(\frac{y + d_{el} + \nu t}{2\sqrt{Dt}}\right)\right]\right) \tag{24}$$

which holds for the boundary conditions

$$\psi(y, t = 0) = \begin{cases} \psi_0 & 0 < y < d_{el} \\ 0 & y \geq d_{el} \end{cases} \tag{25}$$

$$\psi(y = 0, t) = 0, \qquad t > 0 \tag{26}$$

$$\psi(y = \infty, t) = 0, \qquad t > 0 \tag{27}$$

with d_{el} being the thicknesses of the electrolyte ($0 \leq y < d_{el}$).

In eq 24, erfc x is the complementary error function

$$\text{erfc } x = 1 - \frac{2}{\sqrt{\pi}}\int_0^x \exp(-\tau^2)\,d\tau \tag{28}$$

Equation 24 indicates how the concentration of ions varies as a function of time at a fixed position. The total amount of charge $Q_{ion}^{CVG}(t)$ that is transported into the channel can therefore be obtained by inserting eq 24 into eq 23 and integrating over time.

Although eq 24 is mathematically correct, the imposed boundary conditions (eqs 25−27) do not apply for the use of OECTs for the following reasons.

i. Equation 25 assumes a square ion concentration profile and no ions in the semiconductor film. The physical realization of this scenario would be to bring the electrolyte in contact with the semiconductor when the gate voltage is already applied. In practice, however, the semiconductor is typically in contact with the electrolyte before the gate electrode is immersed. Therefore, ions may begin to diffuse into the OMIEC even before the gate voltage is applied.

ii. Equation 26 explicitly assumes that ion concentration near the gate electrode is zero immediately upon application of the gate voltage. Such a sudden change would imply an ion movement into the gate electrode, contradicting the intuitive expectation that ions move in the electric field direction.

iii. Equation 27 implies an open boundary, i.e., an infinitely thick semiconductor ($d_{sc} = \infty$). As can be seen in the results presented by Coppedè et al.,[26] the ion concentration profile leaves completely the electrolyte region, meaning that $Q_{ion}^{CVG}(t \to \infty)$ is independent from the electric field. As a consequence, the CVG model does not allow us to describe the steady state.

iv. Finally, eq 23 explicitly assumes identical diffusivity, standard chemical potential, and electric field in both regions, electrolyte and OMIEC. However, these quantities might be different, and hence, the ion drift−diffusion dynamics differs in the electrolyte and the semiconductor region.

2.3.2. Closed-Boundary DD Model. In order to confine the total ion concentration within a defined region, the closed boundary conditions

$$J(y = 0, t) = 0 \tag{29}$$
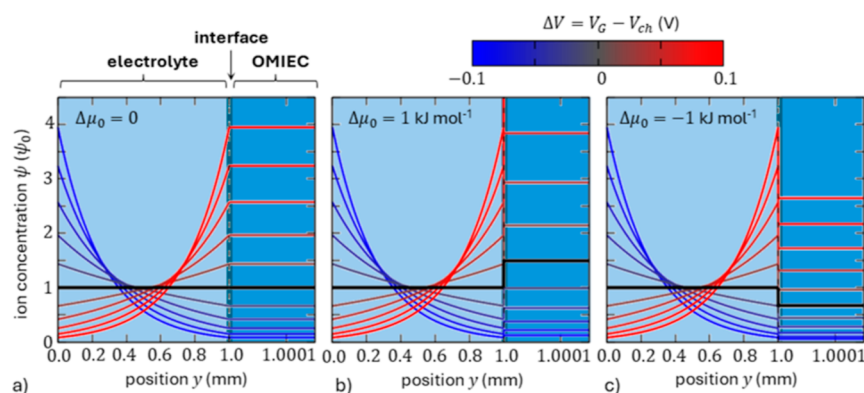
Figure 3. Steady-state profiles of ion concentration along a single device slice with $d_{el} = 1$ mm and $d_{sc} = 150$ nm for $\Delta\mu_0 = 0$ (a), $\Delta\mu_0 > 0$ (b), and $\Delta\mu_0 < 0$ (c). Line colors indicate the voltage difference between the gate and channel according to the color scale. Note that the horizontal scale is stretched by a factor of 3×10^4 in the OMIEC region for proper representation.

$$J(y = d_{el} + d_{sc}, t) = 0 \tag{30}$$

must hold rather than the initial conditions of eqs 25−27 as used in the CVG model.[26] Furthermore, the diffusion and drift properties might be different in the electrolyte and semiconductor. Assuming that the two regions are individually homogeneous, the ion transport in each of them is defined by constant material parameters of diffusion, D_e and D_{sc}, and of standard chemical potential, $\mu_{0,el}$ and $\mu_{0,sc}$. To account for the mix-conductor property of the semiconducting channel, a constant electric potential $\Phi(d_e \leq y < d_{el} + d_{sc}) = V_{ch} = \text{const}$ is considered for the semiconductor region. This assumption is justified for the following reason: Due to the higher electronic mobility compared to that of the ions, a residual electric field in the y-direction inside the semiconducting layer would cause a rearrangement of holes/electrons of the organic film and generate a compensating electric field. This reflects the formation of a double layer at the electrolyte/OMIEC interface.[35,36] Hence, the ion drift perpendicular to the channel direction is zero, such that the ion motion is solely governed by diffusion in the semiconductor region. On the other hand, the electric field within the electrolyte E_{el} ($0 \leq y < d_{el}$) caused by the voltage difference between the gate electrode and the channel is assumed to be homogeneous

$$E_{el}(0 \leq y < d_{el}) = -\frac{\partial\Phi}{\partial y} = \frac{\Delta V}{d_{el}} \tag{31}$$

where $\Delta V = V_G - V_{ch}$. In doing so, our model exhibits a noncontinuous electric field at the interface between the electrolyte and semiconductor.

Under steady-state conditions, i.e., when $\frac{\partial\psi(y,t)}{\partial t} = 0$, eqs 29 and 30 inserted into eq 21 yield $J(y) = 0$. For this case, the differential equation that is obtained when eqs 19, 20, and 31 are inserted into eq 19 can be solved analytically (see Supporting Information, Section S4). The steady-state profile of the ion concentration is obtained as

$$\psi(y) = \begin{cases} \Omega\exp(\lambda(y - d_{el})) & 0 \leq y < d_{el} \\ \Omega\Xi & d_{el} \leq y < d_{el} + d_{sc} \end{cases} \tag{32}$$

with

$$\Omega = \frac{\lambda\psi_0 d_{el}}{1 - \exp(-\lambda d_{el}) + \lambda d_{sc}\Xi} \tag{33}$$

$$\lambda = z\beta\frac{V_G - V_{ch}}{d_{el}} \tag{34}$$

and

$$\Xi = \exp\left(\frac{\Delta\mu_0}{RT}\right) \tag{35}$$

The parameter ψ_0 in eq 33 refers to the homogeneous ion concentration of the electrolyte before contact with the semiconducting layer. Figure 3 displays $\psi(y)$ at steady state for different $\Delta V = V_G - V_{ch}$ values along an OECT cross section for $\Delta\mu_0 = \mu_{0,e} - \mu_{0,sc} = 0$, $\Delta\mu_0 = 1$ kJ mol^{-1}, and $\Delta\mu_0 = -1$ kJ mol^{-1}, respectively. Here, we use $d_{el} = 1$ mm and $d_{sc} = 150$ nm, which are in the order of magnitude of real devices.[21] As expected, for vanishing $\Delta\mu_0$ and $\Delta V = 0$ (Figure 3a, black line), a uniform concentration profile is found. Note that this means that the semiconducting film is slightly loaded with ions that already cause dedoping of the film. For negative ΔV (blue curves), these ions are extracted from the semiconductor and accumulate near the gate contact, presenting an exponentially decaying profile. For $\Delta V > 0$ (red curves), on the other hand, ion migration from the electrolyte into the semiconductor occurs, where again an exponential profile is obtained within the electrolyte region. To reflect the different compositions of the electrolyte and the semiconductor, different values of the standard chemical potentials for each material are now considered, i.e., $\Delta\mu_0 \neq 0$, see Figure 3b,c. Depending on the choice of salt and solvent used for the electrolyte material, ions might favor the environment of the semiconductor over that of the electrolyte or vice versa. For this reason, we consider positive and negative values of $\Delta\mu_0$. For $\Delta\mu_0 \neq 0$ and $V_G = 0$, two different constant concentrations are observed for each region. Due to the favoring of the region of lower standard chemical potential, the so-called "uphill" diffusion effect causes this noncontinuous profile.[37] It is important to mention that under this condition, the total chemical potential $\mu(y)$ takes a constant value for the whole slice, i.e., it is in equilibrium. Depending on whether or not $\mu_{0,e} > \mu_{0,sc}$, the uphill-diffusion effect results in a higher or lower amount of ions inside the semiconductor compared to the case $\mu_{0,e} = \mu_{0,sc}$. For an applied voltage difference ΔV between the gate and the channel position, the concentration profile in the electrolyte exhibits an exponential shape and a constant value in the semiconductor, similarly to the results obtained for $\Delta\mu_0 = 0$.

The ion concentration within the region of the semiconducting film ($t_e \leq y < t_e + t_{sc}$) is now used to determine the total ion charge Q_{ion} that has entered the volume of channel slice $v = W\Delta x t_{sc}$:

$$Q_{ion}(\Delta V) = vez^2 \frac{\psi_0 \beta \Delta V \Xi}{1 - \exp(-z\beta\Delta V) + z\beta\Delta V \frac{d_{sc}}{d_{el}}\Xi} \quad (36)$$

Due to the fact that the semiconductor layer is usually much thinner than the distance between the gate and channel ($d_{sc} \ll d_{el}$), the last term in the denominator of eq 36 can be neglected. The obtained dependence of Q_{ion}^{DD} on the potential difference ΔV can now be inserted into the Bernards–Malliaras assumption of eq 8, resulting in an expression that describes the hole concentration as a function of the channel potential V_{ch} and the applied gate voltage V_G:

$$\rho_h(V_{ch}, V_G) = \rho_0\left(1 - \frac{1}{\Gamma}\frac{z\beta(V_G - V_{ch})}{1 - \exp(-z\beta(V_G - V_{ch}))}\right) \quad (37)$$

with $\Gamma = \frac{\rho_0}{z\psi_0 \Xi}$. As before in the BM model, eq 37 holds only as long as $0 \leq \rho_h \leq \rho_0$. Note that the second term in eq 37 is always positive such that the condition $\rho_h \leq \rho_0$ is automatically fulfilled. The saturation voltage V_{sat}^{DD}, at which $\rho_h = 0$, is given by $V_{sat}^{DD} = V_G - V_P^{DD}$ with the pinch-off voltage being

$$V_P^{DD}(\Gamma) = \frac{1}{z\beta}\{\Gamma + \text{Lambert } W(-\Gamma \exp(-\Gamma))\} \quad (38)$$

A representation of how the quantities ψ_0, ρ_0, and $\Delta\mu$ affect the dimensionless parameter Γ and the pinch-off voltage is presented in Figure S5, see Supporting Information, Section S5. Inserting the expression of eq 37 into eq 4 results in the following expressions of the source drain current:

$$I_D^{DD} = G(V_2 - V_1) + \frac{G}{z\beta\Gamma}[\eta(z\beta(V_G - V_2)) - \eta(z\beta(V_G - V_1))] \quad (39)$$

with

$$\eta(x) = x\ln(1 - \exp x) + \text{Li}_2(\exp(x)) \quad (40)$$

A detailed derivation of eqs 38−40 can be found in the Supporting Information, Section S5, including a schematic illustration of the doping level along the semiconductor channel regarding the four regimes (Figure S6).

We remark that a similar expression as that of eq 37 also makes an appearance in the field of inorganic semiconductors in the form of so-called Fermi−Dirac integrals to treat the effects of doping within Fermi−Dirac statistics.[38] This is worth mentioning, as our eq 37 also describes the effect of doping but in the context of organic semiconductors.

The values of V_1 and V_2 of eq 39 depend on the sequence of V_D and V_G with respect to V_P^{DD}. The different possible cases are summarized in Table 2. The regimes II and IV are the saturation regimes, where I_D^{DD} is independent of V_D. The more important ones are therefore I and III, as they describe the transition between the on-state and the off-state.

3. DISCUSSION

3.1. Transfer and Output Characteristics according to the DD Model. As shown in Figure 4, the transfer and output

Table 2. Overview of the Operational Regimes as Derived for the DD Model

regime			V_1	V_2
I	$V_G < V_P^{DD}$	$V_G - V_P^{DD} < V_D$	0	V_D
II		$V_G - V_P^{DD} > V_D$	0	$V_G - V_P^{DD}$
III	$V_G > V_P^{DD}$	$V_G - V_P^{DD} > V_D$	$V_G - V_P^{DD}$	V_D
IV		$V_G - V_P^{DD} < V_D$	$V_G - V_P^{DD}$	$V_G - V_P^{DD}$

characteristics obtained for eq 39 exhibit the same qualitative features as those found for the BM and the TD models. The transfer curves (Figure 4a) start off with a saturated drain current for strong negative gate voltages, before entering a transition to lower values of $|I_D|$ until converging toward the off-state. While this transition initiates for negative gate voltages when $V_D < 0$, it takes place at about $V_G \approx 0$ for all positive drain voltages. Conversely, the convergence to the off-state is the same for all negative drain voltages, whereas it shifts to larger values for $V_D > 0$. The output characteristics (Figure 4b), on the other hand, also exhibit constant values of I_D before turning into a linear function resampling the behavior of a diode.

As before for the BM model (Table 1) and the TD model (eqs 16 and 17), we consider the dimensionless parameter $\alpha = I_D/GV_D$ to express the change of film conductivity upon the applied electrical conditions. The respective curves as a function of gate and drain are given as insets of Figure 4a,b. The case $V_D \to 0$ is of particular interest, which has only meaningful contributions within regime I:

$$\alpha_{V_D \to 0}^{DD}(V_G) = 1 - \frac{1}{\Gamma}\frac{z\beta V_G}{1 - \exp(-z\beta V_G)}, \qquad V_G < V_P \quad (41)$$

To analyze how the transfer and output curves depend on the model parameter Γ, $\alpha^{DD}(V_G, V_D)$ is plotted in Figure 4c−f. Overall, the same qualitative trends are obtained for all values of Γ but with a stretched or squeezed transition region from the on-state to the off-state. More specifically, the onset voltage where α^{DD} diverges from unity is largely independent from Γ, whereas the convergence to the off-state is shifted. This is in line with the fact that a smaller Γ value corresponds to one of the following cases: (i) a smaller intrinsic hole concentration ρ_0, (ii) a higher salt concentration in the electrolyte ψ_0, or (iii) an increased difference in standard chemical potential $\Delta\mu$. In case (i), the total number of ion charges that has entered the OMIEC for specific electronic conditions is the same, but the dedoping effect is stronger because, loosely speaking, fewer holes have to be replaced by cations, hence the shift to lower voltages. For case (ii), the ion concentration profile in each slice remains, but the absolute scale changes with respect to ψ_0. Hence, more total ion charge entered the semiconductor film, causing a stronger dedoping. Finally, case (iii) refers to the scenario when the cations favor the OMIEC environment over the electrolyte. This means that a larger number of ions enter the semiconducting channel due to drift, and consequently, a lower driving force is required to fully dedope the OMIEC.

3.2. Comparison to Experimental Data. The applicability of the analytical expressions derived from the different models is evaluated by fitting I_D^{BM} (Table 1), I_D^{TD} (eq 14), and I_D^{DD} (eq 39) to experimental data obtained from a simple depletion-mode OECT device using PEDOT:PSS as a
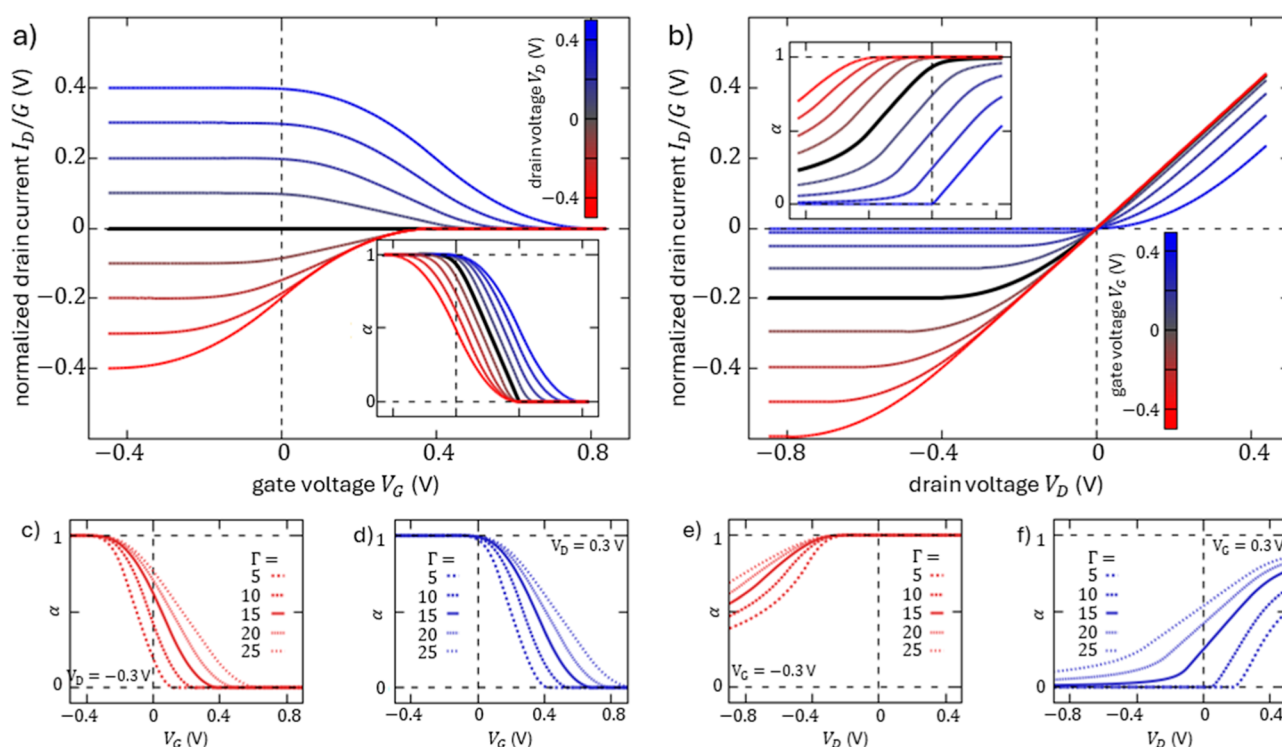
Figure 4. Simulated transfer (a) and output (b) characteristics as obtained from the drift−diffusion model (eq 28). Insets and subfigures (c−f) present graphs of the dimensionless parameter α^{DD} as a function of V_G, V_D, and the model parameter Γ.
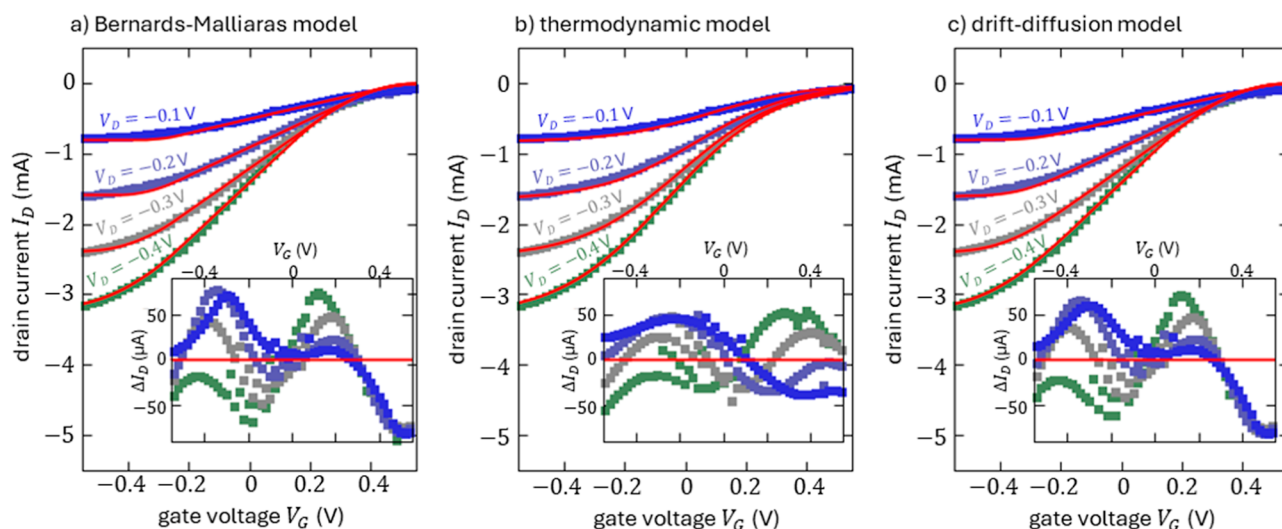
Figure 5. Transfer curves obtained for a PEDOT:PSS-based depletion-mode transistor ($W = 0.5$ cm, $L = 0.5$ cm, $t_{sc} = 200$ nm) using LiCl (200 mM) as an electrolyte. For details on device assembly, see Supporting Information Section S5. Experimental curves are superimposed with fits using the BM model (a, $G^{BM} = 7.93$ mS, $V_p^{BM} = 0.79$ V, $V_{th}^{BM} = -0.241$ V), the thermodynamic model (b, $G^{TD} = 8.25$ mS, $\gamma = 0.16$, $Z = 2.35$), and the drift−diffusion model (c, $G^{DD} = 7.99$ mS, $\Gamma = 30.5$, $V_{th}^{DD} = -0.242$ V) as derived in Sections 2.1, 2.2, and 2.3, respectively. Inset figures present the residuals between fit and measured data.

semiconducting layer and LiCl in H_2O as an electrolyte. For details on device fabrication and the electrical characterization, see Supporting Information, Section S6. To do so, we introduce a threshold voltage V_{th} to the BM and our DD model as it is usually done.[23] This quantity accounts for a gate voltage offset that can be associated with the onset potential at which the electrochemical dedoping reaction occurs,[22] the voltage drop due to contact resistances,[39] or double-layer formation at the gate/electrolyte and electrolyte/semiconductor interface.[36,40] Double-layer formation is a well-documented

phenomenon that occurs at interfaces between different media. It is usually associated with the accumulation of charges on one side of the interface due to the electric field, which induces a polarization in the medium on the other side of the interface.[35] While this phenomenon might vary upon variation of the applied voltages, Weissbach et al. recently demonstrated that devices exhibiting nonpolarizable gates such as Ag/AgCl pallets, as we use in our device, operate with a constant threshold voltage and excellent output saturation.[35] For these reasons, $V_G - V_{th}$ is substituted for V_G in all expressions of
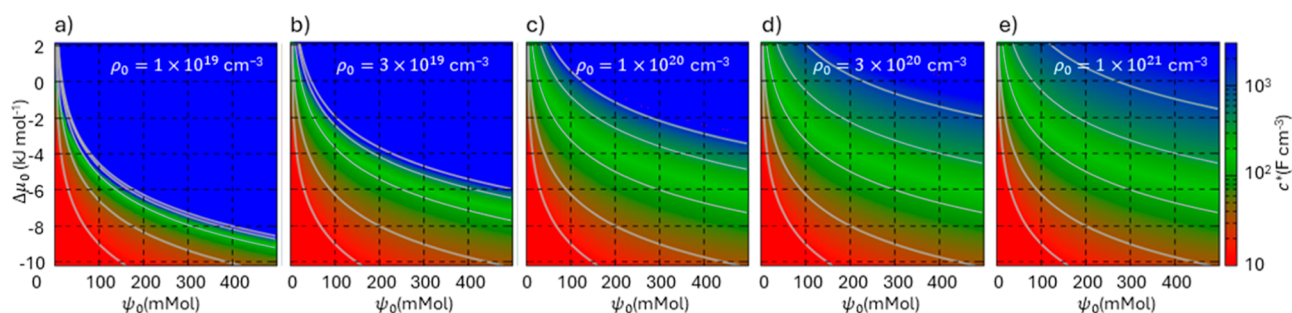
Figure 6. Dependence of volumetric capacitance c^* on the material parameters ψ_0 and $\Delta\mu_0 = \mu_{0,el} - \mu_{0,sc}$ for $\rho_0 = 1 \times 10^{19}$ cm^{-1} (a), for $\rho_0 = 3 \times 10^{19}$ cm^{-1} (b), for $\rho_0 = 1 \times 10^{20}$ cm^{-1} (c), for $\rho_0 = 3 \times 10^{20}$ cm^{-1} (d), and for $\rho_0 = 1 \times 10^{21}$ cm^{-1} (e) as obtained by choosing $V_p^{BM} = V_p^{DD}$. The blue region indicates values $c^* \geq 3 \times 10^3$ F cm^{-1}.

Table 1 and eq 39. For the TD model (eq 16), such a term is not needed because here the parameter Z accounts for this lateral shift of the transfer curves. It is worth mentioning, however, that the effect of double-layer formation will affect this quantity when fitting the model to experimental curves. This renders the interpretation of the electrochemical potential difference between doped and undoped PEDOT in the TD model somewhat questionable.

Figure 5 displays the obtained transfer characteristics superimposed on the individual fit results. We emphasize at this point that these fits were performed for all transfer curves at once rather than individually for each V_D. This is crucial because although fitting the curves individually might improve the quality, it renders their meaning rather insignificant since a dependence of the model parameters on V_D will remain.

The same holds for analyzing output curves. It is common praxis, however, to characterize the OECT parameters by a single curve rather than a more complete scan or fit the curves individually, such as in ref 21.

As one can see in Figure 5, for all three models, a very good agreement with the recorded data is found with similar absolute differences between model expression and measured values. This observation is in sharp disagreement with conclusions drawn by Cucchi et al.,[22] who reported much better agreement for their TD model than for the BM model. This is, however, rather due to inaccurate use of the BM model than to different device or measurement conditions because in their work they applied the expression of regime V (Table 1) for the full range. In Figure S3, we also performed fits for their data and found similarly good agreement for the BM model as well as for the TD model as well as our results. The important message of this comparison is therefore that based on the agreement between theory and experiment, it might be misleading to conclude that the fundamental assumptions of the individual model must be true. In the here presented case, the utilized models are based on different approaches and result in different mathematical expressions, but the overall shapes are nearly identical. One can therefore assume that the physical and chemical processes that govern the response of an OECT are a mixture of the different effects.

3.3. Correlation between Models. The overall good agreement of all models with experimental data presented in Figure 5 and Supporting Information, Section S2, raises the question of how the individual model parameters are correlated to each other. To approach this question, it is meaningful to consider the dimensionless parameter α introduced in eq 6 as it is independent of the geometry of the channel (length, width, and thickness) as well as from hole mobility. For all models, it holds that $0 \leq \alpha \leq 1$, but when and how $\alpha \to 0$ and $\alpha \to 1$ depends on the individual model parameters as well as the applied electrical conditions, i.e., the voltages V_G and V_D. Defining specific conditions under which a certain correlation between the models is expected allows for interconversion expression between the models.

For both the BM and the DD models, the pinch-off voltages V_p^{BM} and V_p^{DD} were introduced, respectively, see eqs 11 and 38. Under the condition $V_D \to 0$, i.e., when the whole channel is at constant potential, it refers to that gate voltage at which the film is fully deleted of holes, i.e., when $\alpha_{V_D \to 0}^{DD}$ vanishes. Choosing the pinch-off voltages of both models to be equal allows us to express the volumetric capacitance c^* of the BM model in terms of the DD parameter Γ:

$$c^* = \rho_0 \frac{ze^2}{k_b T} \frac{1}{\Gamma}\left(1 + \frac{1}{\Gamma} \text{Lambert } W(-\Gamma \exp(-\Gamma))\right)^{-1} \tag{42}$$

This relationship between c^* and Γ, i.e., the DD model parameters ψ_0, ρ_0, and $\Delta\mu_0$, is presented in Figure 6. It shows that for ion concentrations between 0.1 and 0.5 M and hole concentrations between 10^{19} and 10^{21} cm^{-3}, the predicted values of c^* lay in the range of 10 until 10^3 F cm^{-3}. These values are in the order of magnitude, as reported in literature.[41]

How choosing $V_p^{BM} = V_p^{DD}$ reflects in transfer curves obtained from the BM and the DD models is presented in Figure 7. As one can see in Figure 7a, matching curves are obtained for $\alpha_{V_D \to 0}^{BM}$ and $\alpha_{V_D \to 0}^{DD}$ for $V_G > 0.1$ V. For negative gate voltages, on the other hand, the two curves slightly differ. While the DD model presents a smooth convergence to $\alpha = 1$ as $V_G \to -\infty$, $\alpha_{V_D \to 0}^{BM}$ remains equal to 1 for all negative gate voltages and exhibits a sharp kink at $V_G = 0$, see the inset of Figure 6a. This is due to the fact that the BM model only considers ions to enter the semiconducting film upon application of a gate voltage and therefore fails in describing the dedoping associated with the diffusion due to the gradient in electrochemical potential at the interface. As V_G becomes larger, the number of ions entering the semiconductor due to the drift becomes dominant, which is equally described in both models. Hence, the BM model is a limit of the DD model. As shown in Figure 6b, the agreement between the two models, when setting the two pinch-off voltages to be equal, extends beyond $V_D \to 0$ and is even improved as the absolute difference $\alpha^{DD} - \alpha^{BM}$ decreases (see the inset of Figure 7b). This is in line with the expectation that for nonzero V_D, an electric field acts between the gate and channel, rendering the drift effects more dominant.
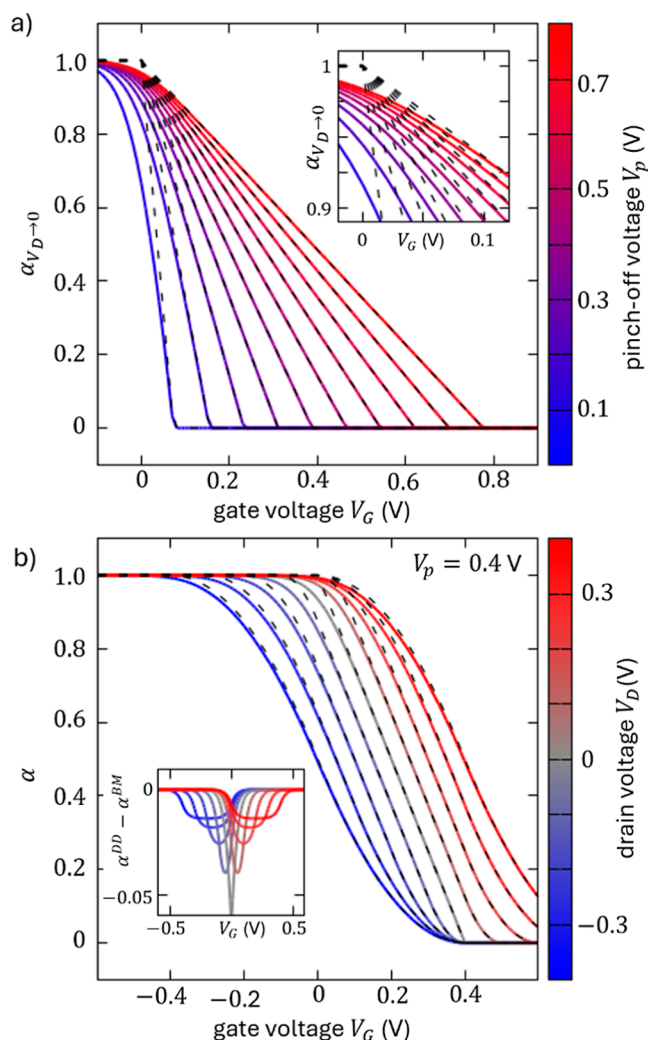
Figure 7. Dependence of α^{DD} and α^{BM} on gate voltage V_G, drain voltage V_D, and pinch-off voltage V_p as obtained from the drift–diffusion model (colored curves) and the BM model (dashed lines) when choosing V_p to be equal in both models. Subfigure (a) illustrates the $\alpha_{V_D \rightarrow 0}$ for different values of V_p, whereas subfigure (b) compares α^{BM} to α^{DD} for different V_D.

According to our DD model, V_p^{DD} increases for higher ion concentrations ψ_0 (see Figure S4), which results in shifted transfer curves as suggested by Figure 7a. This is in line with results published by Romele et al., who present transfer curves for PEDOT:PSS-based OECTs using NaCl solutions at different concentrations as an electrolyte.[39] Conversely to our model, they correlate this shift solely to the threshold voltage due to changes in the potential drop at the gate/electrolyte and electrolyte/semiconductor rather than to a change in the pinch-off voltage. When overlaying their recorded curves, however, it becomes evident that the S-shape of the transfer curve changes and that the convergence to the saturation current is slightly slower for higher ion concentrations in the electrolyte. The same trend is predicted from our model. We therefore conclude that the potential drop at the interface does not fully explain the responses of real OECTs and that the BM model as used by Romele et al. does not allow us to fully investigate this effect.

Our drift–diffusion model furthermore suggests that V_p increases for smaller values of $\Delta\mu_0 = \mu_{0,el} - \mu_{0,sc}$, i.e., the more the ions prefer the electrolyte over the semiconductor. According to the BM model, on the other hand, V_p is inversely proportional to the volumetric capacitance c^*. Combining the two trends suggests that c^* decreases for smaller $\Delta\mu_0$, see Figure 6. A confirmation of this can be found in the literature of OECTs. Among other effects, Inal et al. studied the dependency of PEDOT:PSS-based depletion-mode OECTs, where different amounts of ethylene glycol (EG) were admixed to the semiconductor. In their work, they report that for higher EG content, the volumetric capacitance drops.[41] Since the solubility of sodium in EG is smaller than in water,[42] one can conclude that adding EG to PEDOT:PSS increases $\Delta\mu_{0,sc}$ and therefore reduces c^*. Hence, our model can attribute some physical and chemical fundamentals to the experimentally obtained trends of the volumetric capacitance. This possibility to link the insights from our novel description to the frequently reported agreement between experimental measurements and the capacitive model is advantageous compared with other alternative models of the OECTs. Looking for conversion formulas between the TD and the BM model using symmetry properties of the two descriptions results in a contradiction of the fundamental meaning of the individual model parameters, see Supporting Information, Section S7. For example, a dependence of the empirical TD parameter γ on the drain voltage is found, which shows approximately constant behavior for small values of V_D and sufficiently large V_p^{BM} but a strong divergence elsewhere, see Figure S7.

4. CONCLUSIONS

In this work, we have advanced our understanding of organic electrochemical transistor (OECT) models through a comprehensive analysis and discussion of steady-state I–V characteristics. We extended the frameworks proposed by Bernards and Malliaras by developing expressions for the drain current that encompass the entire range of gate and drain voltages. Additionally, we critically examined a recent TD model for OECTs, enhancing our understanding of its implications and limitations. Furthermore, a novel drift–diffusion-based model was introduced, offering insights into the physical and chemical fundamentals influencing the device's behavior. Through rigorous comparison with experimental data, including our own measurements as well as literature data sets, we demonstrated the efficacy of each model in accurately resampling transfer curves, rendering the match itself an insufficient proof of the underlying theory. Having found that all models agree to experiment to a similar extent, although being based on fundamentally different concepts, we developed interconversion formulas to translate the parameters of one model into another, thereby facilitating a unified understanding of different theoretical approaches. By relating the volumetric capacitance, a fundamental quantity in the Bernards and Malliaras model, to parameters in our drift–diffusion model, we provided a deeper physical interpretation of observed trends reported in the literature over the past decade.

Looking forward, several avenues for future research emerge from our findings. While our work utilizes a continuum approach, in which the nanoscale features are merged into simple material parameters, in particular, the electrochemical potential and diffusion constants, future works should focus on how properties at the nanolevel such as composition and morphology at the molecular scale affect these physical constants. Therefore, incorporating nanoscale design parame-

ters may further enhance the theoretical modeling and, thus, drive the development of devices with improved performances. Moreover, future works should extend our derived equations to encompass accumulation-mode OECTs and accommodate semiconducting materials of n-type conductivity, as well as explore the behavior of ambipolar organic mixed ionic−electronic conductors. It is suggested to systematically analyze further existing literature data on OECTs utilizing the interconversion formulas and look for a fundamental interpretation of the volumetric capacitance in terms of the material parameters rather than pure device parameters. Further experimental studies should aim to capture a broader range of operating conditions and material characteristics, providing a more comprehensive data set for model validation and refinement. In particular, devices utilizing polarizable electrodes might be of interest for confirming the effects of variable threshold voltages. Finally, moving beyond steady-state analysis, future research should take transient descriptions into account, where diffusion effects play a more prominent role, offering deeper insights into device dynamics and performance under dynamic operating conditions. By pursuing these avenues, we anticipate advancing both the theoretical foundations and practical applications of organic electrochemical transistors, paving the way for their integration into next-generation electronic and bioelectronic devices.

■ ASSOCIATED CONTENT

Supporting Information

The Supporting Information is available free of charge at https://pubs.acs.org/doi/10.1021/acsanm.5c02101.

> List of symbols, operational regimes of the BM model, empirical correction factor of the thermodynamic model, steady-state ion-concentration profile, analytical expression for the steady-state drain current, experimental details, and correlating BM and thermodynamic models (PDF)

■ AUTHOR INFORMATION

Corresponding Author

Florian Günther − *Instituto de Física de São Carlos, Universidade de São Paulo, São Carlos 13566-590, Brazil; Departamento de Física, Instituto de Geociências e Ciências Exatas, Universidade Estadual Paulista, Rio Claro 13506-900, Brazil;* orcid.org/0000-0001-5002-4172; Email: florian.gunther@unesp.br

Author

Andres Unigarro − *Institut für Physik, Technische Universität Chemnitz, Chemnitz 09111 Saxony, Germany; Instituto de Física de São Carlos, Universidade de São Paulo, São Carlos 13566-590, Brazil;* orcid.org/0009-0002-3283-5283

Complete contact information is available at:
https://pubs.acs.org/10.1021/acsanm.5c02101

Author Contributions

The manuscript was written through contributions of all authors. All have given approval to the final version of the manuscript.

Notes

The authors declare no competing financial interest.

■ ACKNOWLEDGMENTS

■ ABBREVIATIONS

OECT, organic electrochemical transistor; OMIEC, organic mixed ionic−electronic conductor; PEDOT, poly-3,4-ethylendioxythiophen; PSS, polystyrenesulfonate; BM, Bernards−Malliaras; TD, thermodynamic; CVG, Coppedè−Villani−Gentile; DD, drift−diffusion

■ REFERENCES

(1) Paudel, P. R.; Kaphle, V.; Dahal, D.; Radha Krishnan, R. K.; Lüssem, B. Tuning the Transconductance of Organic Electrochemical Transistors. *Adv. Funct. Mater.* **2021**, *31* (3), 2004939.

(2) Paudel, P. R.; Tropp, J.; Kaphle, V.; Azoulay, J. D.; Lüssem, B. Organic Electrochemical Transistors − from Device Models to a Targeted Design of Materials. *J. Mater. Chem. C* **2021**, *9* (31), 9761−9790.

(3) Rivnay, J.; Inal, S.; Salleo, A.; Owens, R. M.; Berggren, M.; Malliaras, G. G. Organic Electrochemical Transistors. *Nat. Rev. Mater.* **2018**, *3* (2), 17086.

(4) Nilsson, D.; Robinson, N.; Berggren, M.; Forchheimer, R. Electrochemical Logic Circuits. *Adv. Mater.* **2005**, *17* (3), 353−358.

(5) Gkoupidenis, P.; Schaefer, N.; Strakosas, X.; Fairfield, J. A.; Malliaras, G. G. Synaptic Plasticity Functions in an Organic Electrochemical Transistor. *Appl. Phys. Lett.* **2015**, *107* (26), 263302.

(6) Amanchukwu, C. V.; Gauthier, M.; Batcho, T. P.; Symister, C.; Shao-Horn, Y.; D'Arcy, J. M.; Hammond, P. T. Evaluation and Stability of PEDOT Polymer Electrodes for Li−O 2 Batteries. *J. Phys. Chem. Lett.* **2016**, *7* (19), 3770−3775.

(7) Lin, P.; Yan, F. Organic Thin-Film Transistors for Chemical and Biological Sensing. *Adv. Mater.* **2012**, *24* (1), 34−51.

(8) Bernards, D. A.; Malliaras, G. G. Steady-State and Transient Behavior of Organic Electrochemical Transistors. *Adv. Funct. Mater.* **2007**, *17* (17), 3538−3544.

(9) Marquez, A. V.; McEvoy, N.; Pakdel, A. Organic Electrochemical Transistors (OECTs) Toward Flexible and Wearable Bioelectronics. *Molecules* **2020**, *25* (22), 5288.

(10) Song, J.; Li, L.; Wong, W.-Y.; Yan, F. Organic Mixed Conductors in Electrochemical Transistors for Bioelectronic Applications. *Acc. Mater. Res.* **2024**, *5* (9), 1036−1047.

(11) Tropp, J.; Meli, D.; Rivnay, J. Organic Mixed Conductors for Electrochemical Transistors. *Matter* **2023**, *6* (10), 3132−3164.

(12) Lang, U.; Müller, E.; Naujoks, N.; Dual, J. Microscopical Investigations of PEDOT:PSS Thin Films. *Adv. Funct. Mater.* **2009**, *19* (8), 1215−1220.

(13) Timpanaro, S.; Kemerink, M.; Touwslager, F. J.; De Kok, M. M.; Schrader, S. Morphology and Conductivity of PEDOT/PSS Films Studied by Scanning−Tunneling Microscopy. *Chem. Phys. Lett.* **2004**, *394* (4−6), 339−343.

(14) Sun, K.; Zhang, S.; Li, P.; Xia, Y.; Zhang, X.; Du, D.; Isikgor, F. H.; Ouyang, J. Review on Application of PEDOTs and PEDOT:PSS in Energy Conversion and Storage Devices. *J. Mater. Sci. Mater. Electron.* **2015**, *26* (7), 4438−4462.

(15) Friedlein, J. T.; McLeod, R. R.; Rivnay, J. Device Physics of Organic Electrochemical Transistors. *Org. Electron.* **2018**, *63*, 398−414.

(16) Savva, A.; Hallani, R.; Cendra, C.; Surgailis, J.; Hidalgo, T. C.; Wustoni, S.; Sheelamanthula, R.; Chen, X.; Kirkus, M.; Giovannitti,

A.; Salleo, A.; McCulloch, I.; Inal, S. Balancing Ionic and Electronic Conduction for High-Performance Organic Electrochemical Transistors. *Adv. Funct. Mater.* 2020, 30 (11), 1907657.

(17) Hu, Z.; Hu, Y.; Huang, L.; Zhong, W.; Zhang, J.; Lei, D.; Chen, Y.; Ni, Y.; Liu, Y. Recent Progress in Organic Electrochemical Transistor-Structured Biosensors. *Biosensors* 2024, 14 (7), 330.

(18) Ding, B.; Jo, I.-Y.; Yu, H.; Kim, J. H.; Marsh, A. V.; Gutiérrez-Fernández, E.; Ramos, N.; Rapley, C. L.; Rimmele, M.; He, Q.; Martín, J.; Gasparini, N.; Nelson, J.; Yoon, M.-H.; Heeney, M. Enhanced Organic Electrochemical Transistor Performance of Donor–Acceptor Conjugated Polymers Modified with Hybrid Glycol/Ionic Side Chains by Postpolymerization Modification. *Chem. Mater.* 2023, 35 (8), 3290–3299.

(19) Flagg, L. Q.; Cho, W.; Woodcock, J.; Li, R.; Ro, H. W.; Delongchamp, D. M.; Richter, L. J. Improved Organic Electrochemical Transistors via Directed Crystallizable Small Molecule Templating. *Chem. Mater.* 2024, 36 (3), 1352–1361.

(20) Chen, S.; Surendran, A.; Wu, X.; Lee, S. Y.; Stephen, M.; Leong, W. L. Recent Technological Advances in Fabrication and Application of Organic Electrochemical Transistors. *Adv. Mater. Technol.* 2020, 5 (12), 2000523.

(21) Colucci, R.; Feitosa, B. d. A.; Faria, G. C. Impact of Ionic Species on the Performance of Pedot:PSS-Based Organic Electrochemical Transistors. *Adv. Electron. Mater.* 2024, 10 (2), 2300235.

(22) Cucchi, M.; Weissbach, A.; Bongartz, L. M.; Kantelberg, R.; Tseng, H.; Kleemann, H.; Leo, K. Thermodynamics of Organic Electrochemical Transistors. *Nat. Commun.* 2022, 13 (1), 4514.

(23) Colucci, R.; Barbosa, H. F. D. P.; Günther, F.; Cavassin, P.; Faria, G. C. Recent Advances in Modeling Organic Electrochemical Transistors. *Flexible Printed Electron.* 2020, 5 (1), 013001.

(24) Friedlein, J. T.; Shaheen, S. E.; Malliaras, G. G.; McLeod, R. R. Optical Measurements Revealing Nonuniform Hole Mobility in Organic Electrochemical Transistors. *Adv. Electron. Mater.* 2015, 1 (11), 1500189.

(25) Nissa, J.; Janson, P.; Simon, D. T.; Berggren, M. Expanding the Understanding of Organic Electrochemical Transistor Function. *Appl. Phys. Lett.* 2021, 118 (5), 053301.

(26) Coppedè, N.; Villani, M.; Gentile, F. Diffusion Driven Selectivity in Organic Electrochemical Transistors. *Sci. Rep.* 2014, 4 (1), 4297.

(27) Barbosa, H. F. P.; Higuita, G. D. G.; Günther, F.; Faria, G. C. Tunable Charge-Density PEDOT:PSS for Application in Post-Synaptic Organic Neuromorphic Electrodes. *Adv. Electron. Mater.* 2022, 8 (2), 2100864.

(28) Prigodin, V. N.; Hsu, F. C.; Park, J. H.; Waldmann, O.; Epstein, A. J. Electron-Ion Interaction in Doped Conducting Polymers. *Phys. Rev. B: Condens. Matter Mater. Phys.* 2008, 78 (3), 035203.

(29) Pecqueur, S.; Guérin, D.; Vuillaume, D.; Alibart, F. Cation Discrimination in Organic Electrochemical Transistors by Dual Frequency Sensing. *Org. Electron.* 2018, 57, 232–238.

(30) Bitton, S.; Tessler, N. Unveiling the Impact of the Electrolyte's Counter Ions on Organic Electrochemical Transistor Performance. *Adv. Electron. Mater.* 2024, 10 (6), 2300766.

(31) Flagg, L. Q.; Bischak, C. G.; Onorato, J. W.; Rashid, R. B.; Luscombe, C. K.; Ginger, D. S. Polymer Crystallinity Controls Water Uptake in Glycol Side-Chain Polymer Organic Electrochemical Transistors. *J. Am. Chem. Soc.* 2019, 141 (10), 4345–4354.

(32) Flagg, L. Q.; Giridharagopal, R.; Guo, J.; Ginger, D. S. Anion-Dependent Doping and Charge Transport in Organic Electrochemical Transistors. *Chem. Mater.* 2018, 30 (15), 5380–5389.

(33) Cendra, C.; Giovannitti, A.; Savva, A.; Venkatraman, V.; McCulloch, I.; Salleo, A.; Inal, S.; Rivnay, J. Role of the Anion on the Transport and Structure of Organic Mixed Conductors. *Adv. Funct. Mater.* 2019, 29 (5), 1807034.

(34) Newman, J.; Thomas-Alyea, K. E. *Electrochemical Systems*; The ECS Series of Texts and Monographs; Wiley, 2004.

(35) Weissbach, A.; Cucchi, M.; Tseng, H.; Leo, K.; Kleemann, H. Unraveling the Electrochemical Electrode Coupling in Integrated Organic Electrochemical Transistors. *Adv. Funct. Mater.* 2023, 33 (46), 2302205.

(36) Shin, S.-J.; Kim, D. H.; Bae, G.; Ringe, S.; Choi, H.; Lim, H.-K.; Choi, C. H.; Kim, H. On the Importance of the Electric Double Layer Structure in Aqueous Electrocatalysis. *Nat. Commun.* 2022, 13 (1), 174.

(37) Darken, L. Diffusion of Carbon in Austenite with a Discontinuity in Composition. *Metall. Mater. Trans. A* 2010, 41, 1607–1615.

(38) Goano, M. Series Expansion of the Fermi–Dirac Integral over the Entire Domain of Real j and X. *Solid State Electron.* 1993, 36 (2), 217–221.

(39) Romele, P.; Ghittorelli, M.; Kovács-Vajna, Z. M.; Torricelli, F. Ion Buffering and Interface Charge Enable High Performance Electronics with Organic Electrochemical Transistors. *Nat. Commun.* 2019, 10 (1), 3044.

(40) Islam, M. M.; Ohsaka, T. Electrical Double Layer at Electrode/Ionic Liquid Interfaces. In *Encyclopedia of Solid-Liquid Interfaces*; Elsevier, 2024; pp 40–51.

(41) Inal, S.; Malliaras, G. G.; Rivnay, J. Benchmarking Organic Mixed Conductors for Transistors. *Nat. Commun.* 2017, 8 (1), 1–6.

(42) Trimble, H. M. Solubilities of Salts in Ethylene Glycol and in Its Mixtures with Water. *Ind. Eng. Chem.* 1931, 23, 165–167.